A tale of two tails: Developing an avian inspired morphing actuator for yaw control and stability

Lawren L. Gamble[1] and Daniel J. Inman[2]

[1,2]Department of Aerospace Engineering, University of Michigan, Ann Arbor, USA

Abstract

Motivated by the lack of research in tailless morphing aircraft in addition to the current inability to measure the resultant aerodynamic forces and moments of bird control maneuvers, this work aims to develop and test a multi-functional morphing control surface based on the horizontal tail of birds for a low-radar-signature UAV. Customized Macro Fiber Composite (MFC) actuators were designed to achieve yaw control across a range of sideslip angles by inducing three dimensional curvature as a result of bending twisting coupling, a well-known phenomenon in classical fiber composite theory. This allows for yaw control, pitch control, and limited air break control. The structural response of the customized actuators was determined numerically using both a piezoelectric and an equivalent thermal model in order to optimize the fiber direction to allow for maximized deflection both normal and orthogonal to the freestream velocity. In total, three configurations were tested experimentally: symmetric deflection for pitch control, single deflection for yaw control, and antisymmetric deflection for air brake control. A Reynolds-averaged-Navier-Stokes (RANS) fluid simulation was also developed to validate the experimental results for the unactuated baseline configuration. The actuator was shown to provide better yaw control to traditional split aileron methods, remain effective in larger sideslip angles, and provide directional yaw stability when unactuated. Furthermore, it was shown to provide adequate pitch control in sideslip in addition to limited air brake capabilities. This design is proposed to provide complete aircraft control in concert with spanwise morphing wings.

1 Introduction

The field of morphing aircraft has recently gained tremendous momentum due to the monetary and environmental benefits of reduced fuel consumption, the development of new active and compliant materials, and advancements in understanding the mechanics of avian flight. Birds in particular provide a unique opportunity for the aerospace community to draw inspiration from when designing small unmanned aerial vehicles (UAVs) as they operate in similar aerodynamic conditions. Birds exhibit tremendous maneuverability and stability, in part because they drastically morph their geometry with both large scale and fine-tuned maneuvers [1] [2] [3]. Like aircraft, the cambered wings generate the majority of the total lift during soaring maneuvers, but the tail performs rapid fine tuned movements including pitch, twist and spread to stabilize the body in gusty conditions [2] [4]. The role of the horizontal tail in particular is crucial, as it contributes to both static yaw and directional stability [5], dynamic corrective stabilization, and complete attitude control. The geometry of the tail itself provides static stability due to its

asymmetric drag contribution aft of the center of gravity during sideslip which provides a restoring moment. This allows birds to have relatively unswept wings in gliding flight without sacrificing yaw stability, a configuration which tailless aircraft cannot afford. This adaptability gives birds an edge over traditional aircraft.

1.1 Yaw Control

Although small UAVs encounter similar aerodynamic challenges as natural fliers due to their comparable geometry, size and weight; they rarely incorporate bioinspired designs. Many small-scale UAVs use traditional yaw control methods such as vertical stabilizers and rudders like the Elbit Skylark, RQ-11 Raven, and Desert Hawk [6], which add drag and increase the aircraft's radar signature. This is drastically different from previous efforts in tailless or flying wing designs in transonic aircraft, such as the X-45C and the B-2. Here, tailless aircraft are defined by their lack of a vertical stabilizer. Without a vertical stabilizer, these aircraft actively control yaw using split ailerons or spoilers [7] [8] and rely a swept wing configuration to provide static yaw stability. Scaling down these designs to the size of a small UAV or bird introduces additional complexities regarding stability and control, as these aircraft are designed specifically for efficient high altitude and high speed flight. At low altitudes where low-speed fliers typically operate, wind gusts are non-biased in direction and can exceed the magnitude of the flight velocity which can cause the bird or UAV to experience substantial sideslip. In current tailless or flying wing designs, this could be devastating and can cause loss of aileron authority [9].

1.2 Bioinspired Morphing

While early aircraft designs such as the Wright Flier relied heavily upon observations drawn from natural fliers and involved concepts such as wing warping and camber morphing, existing aircraft and UAVs have veered away from bioinspired shape change. The field of bioinspired morphing aircraft structures represents a modern push towards adaptive flight to increase performance and efficiency. The majority of this effort has focused on the wings due to their role as the primary lifting surface, and has seen the emergence of innovative developments such as twist, sweep, span, thickness, and camber morphing mechanisms [10]. One such development is the cascading bimorph concept which uses piezoelectric smart materials called Macro Fiber Composites (MFCs) to achieve a smooth camber morphing aileron which has been proven to be more effective than traditional ailerons [11]. This concept was later used by Pankonien et al. in the Spanwise Morphing Trailing Edge concept (SMTE) which achieves continuous camber morphing along the wingspan by using multiple camber morphing sections, connected with flexible honeycomb transition sections [12] [13] [14]. This design allows the wing shape to be tailored to adapt to aerodynamic disturbances including stall recovery. Wing morphing has also bridged into the industry sector with the Mission Adaptive Compliant Wing, a retrofit design by FlexSys which uses a compliant mechanism to bridge the gap between an actuated control surface and the wing surface [15]. This eliminates vortex formations at the wing's geometric discontinuities and reduces drag in the process.

However, a limited amount of research has been dedicated to morphing tailless aircraft which are more representative of their biological counterparts which lack a vertical tail and are desirable in stealth operations due to their reduced radar signature. In academia, this research has mainly focused on applying wing morphing technologies, such as those mentioned prior, to tailless aircraft [16]. More large-scale forms of morphing tailless aircraft include the Lockheed-

Martin Agile Hunter which achieves changes in span via large scale folding mechanisms to tailor the geometry for loitering and dash maneuvers [17]. But these designs do not address the lack of directional instability in tailless or flying wing aircraft, inherent coupled effects of having all control surfaces on the lifting surface, and the frequently slow actuation response of large-scale morphing mechanisms. These designs are more practical for transitioning between two flight regimes as opposed to adapting to adverse aerodynamic conditions. Accordingly, this work aims to develop a new method of yaw control for morphing tailless UAVs which addresses some of the pitfalls of current tailless designs discussed prior, and also informs current biological studies by providing insight into the force/moment response of the active horizontal tail of birds.

2 Morphing Tailless Aircraft Concept

The proposed design utilizes a bioinspired horizontal control surface or 'tail' for small UAVs which is designed with two custom MFCs, one on each half of the tail. While this design is still considered tailless since it lacks a vertical stabilizer, the term 'tail' in the current work is used as a comparison to bird anatomy. This tail-like actuator aims to address the lack of directional stability of flying wings by capitalizing on the stability characteristics of the tail of birds. The tail acts as a high aspect ratio control surface aft of the center of gravity which provides a restoring moment in sideslip [4]. As in traditional aircraft, this control surface decouples control from the wings, the main lifting surface. In the current design, the wings maintain lift during gliding flight while the piezoelectric tail actuator undergoes large scale deformations to control pitch and yaw, or it can utilize continuous corrective input to dynamically stabilize the body to the rapid actuation time of the MFC's. Lastly, by implementing MFCs with a custom geometry and fiber orientation, this design proves to be multifunctional and effective over a range of sideslip angles.

The customized fiber orientation is key to the multifunctionality and control robustness of this design. The MFCs are composed of thin PZT fibers which elongate in the fiber direction in the presence of an electric field. When bonded to a thin rigid substrate such as aluminum shim, the structure's neutral axis is shifted which results in curved deformation upon actuation. Using fundamental fiber composite theory, the MFCs will experience bending-twisting coupling if the fiber direction is rotated in plane. This mechanism, which effectively generates displacements in 3D as opposed to 2D in the case of camber morphing MFC actuators, is meant to resemble the actuation authority of bird tails in a more simplified albeit coupled manner which can pitch and rotate. This design provides an advantage over traditional yaw steering control surfaces due to the nature of its complex curvature. Unlike traditional flat control surfaces, whose area perpendicular to the wind vector will decrease with sideslip, the 3D deformation of this actuator retains surface area perpendicular to the flow even at large angles of sideslip as can be seen in Fig. 1.

While typical morphing airfoil studies are frequently conducted on 2D wing sections, the control surface proposed here cannot be approximated as two-dimensional and requires integration into a full aircraft body to study the full 3D effects due to the asymmetric nature of actuation. Accordingly, the aircraft body was designed using the same planform shape as the studies conducted by Hummel and Sachs, *et al.* as shown in Fig. 1a with an actuated control surface. The wing geometry was designed with a symmetric NACA0012 airfoil to eliminate the wing effects on lift, drag and pitching moment. The aircraft was designed to be a half scale model with a wingspan approximately 0.3 m in wingspan. Furthermore, the 3D deformation of the MFCs allow for the control surfaces to remain entirely continuous. This continuity eliminates the formation of vortices which develop at geometric discontinuities and increase drag in traditional

discrete control surface designs [18] [14] [12]. Ultimately, this actuation mechanism would be incorporated in an aircraft along with the spanwise morphing capabilities of the SMTE in the wings to provide complete aircraft control coupled with a sensor network to monitor the mechanical and aerodynamic status of the aircraft and inform the response of the actuators.

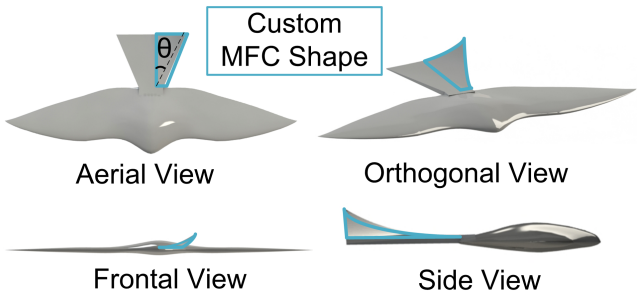

Figure 1. Demonstration of the bioinspired aircraft with left actuator deflected

3 Numerically Solving for Deformed Geometry

In order to determine the the appropriate fiber direction to produce maximized transverse bending-twisting coupling, a numerical model is required which accurately predicts the response of the MFCs. Unlike standard PZT actuators, the MFC's are composed of layers of PZT fibers, electrodes, adhesive and polymer in order to achieve its uniquely flexible characteristics. See Table 1 for the MFC material properties. It is important to note that the dielectric coefficients reported here are specific to the Navy type II PZT used in the MFC, and do not represent the total dielectric coefficients of the MFC itself. Two models are tested here in ABAQUS: a specialized method which accounts for the MFC's modular structure [19], and a thermal analogy [20].

Table 1: Material Properties of M-8557-P1

Properties	MFC
E_1 (GPa)	30.34
E_2 (GPa)	15.86
ν_{12}	.31
G_{12} (GPa)	5.52
l (mm)	85
w (mm)	57
t (mm)	0.3
d_{33} (m/V)	$460e^{-12}$
d_{31} (m/V)	$-210e^{-12}$

3.1 Piezoelectric Model

Here, the piezoelectric material is assumed to be transversely isotropic and the response to an applied electric field is assumed to be linear as is common in basic IEEE standards [21]. For relatively low electric fields, this assumption produces fairly accurate results. The constitutive relations are written as a set of two matrix equations representing the electrical and mechanical components of the actuator's response. The matrix equations are written as:

$$\{\varepsilon\} = [S^E]\{\sigma\} + [d]^T\{D\} \quad (1)$$

$$\{D\} = [d]\{\sigma\} + [\zeta^\sigma]\{E\} \quad (2)$$

where S^E is the material compliance in constant electric field condition, ε is the strain, σ is the stress, d is the piezoelectric coefficient, D is the electric displacement, E is the electric field, and ζ^σ is the permittivity coefficient.

To validate the model a standard M8557-P1 MFC was used which exhibits a d33 –effect. Due to its modular structure, the MFC consists of many small actuators which are defined by the PZT fiber between a pair of interdigitated electrodes. Each actuator unit is thus measured as the distance between the center of the interdigitated electrodes (500μm) minus the width of the electrode (80μm). The total number of actuator units in the MFC is determined by dividing the total active length of the MFC by the actuator unit width. As the electrode pitch across all manufactured MFCs is constant, all MFCs of the same length will have an equal number of units. For example, as the M8557-P1 MFC has an active length of 85mm, it would be composed of 202 PZT units. The the total dielectric coefficient of the MFC is calculated by multiplying the reported piezoelectric constant for the Navy type II PZT by the total number of units. This process was repeated in order to calculate the MFC's d_{31} coefficient as well. In the model, the standard C3D20E piezoelectric element was used which contains 4 degrees of nodal freedom: one electric charge, and 3 translations. Lastly, the electric field was applied via a voltage boundary condition with one edge receiving 0V and the opposite edge receiving 1500V.

3.2 Thermal Model

The MFCs can also be modeled using a thermal analogy which draws parallels between an electrically actuated MFC and a thermally expanding transversely isotropic material. The analogy relates the electric field applied to the MFC to the thermal load, and the piezoelectric coefficients to the thermal expansion coefficients. Accordingly, the piezoelectric (left) and thermal (right) constitutive relations can be related as such

$$\{\varepsilon\} = [S^E]\{\sigma\} + \{d^T\}\frac{\psi_3}{b} = [S]\{\sigma\} + \{\alpha\}\,\Delta T \quad (3)$$

where ψ_3 is the potential voltage difference between electrodes, b is the spacing between electrodes, ΔT is the change in temperature, and α is the thermal expansion coefficient. The piezoelectric coefficient is directly analogous with the piezoelectric coefficients (i.e. $\alpha_{13} = d_{13}$ and $\alpha_{33} = d_{33}$) while the electric field applied to the MFC is analogous to the ratio of the voltage potential to the electrode spacing $\frac{\psi_3}{b}$. To model the MFC as opposed to an individual PZT electrode pair, b is taken to be the total active length of the MFC and ψ_3 is taken to be the applied voltage. In this model, C3D8R general purpose linear brick element was used. Lastly, the thermal load is applied in the form of a constant predefined field as opposed to a boundary condition.

3.3 FEM Results

In order to determine the model's accuracy, the free-strain and blocking force were calculated numerically and compared to the manufacturer's reported values. The free strain, as the name implies, is a measure of the axial strain experienced by the actuator when the maximum voltage is applied without constraints in the axial direction. Conversely, the blocking force is a measure of the axial force output by the actuator when axial deformation is restricted. The boundary conditions required in each of these tests are described in Figure 2. A comparison between the piezoelectric and thermal analysis can be found below in Table 2.

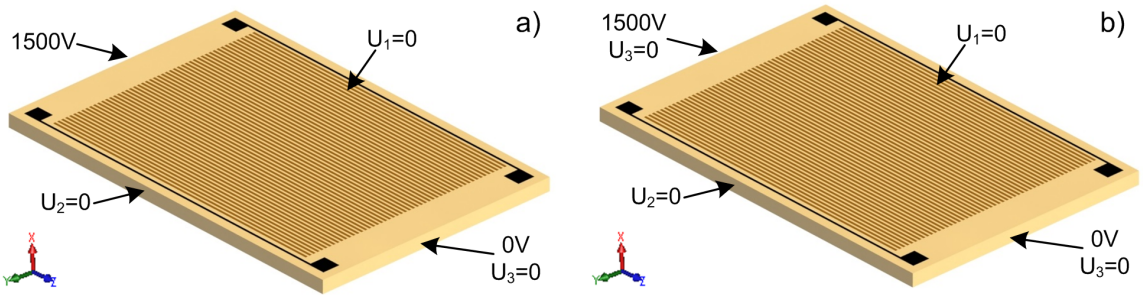

Figure 2: Enforced boundary conditions on the MFC, thickness emphasized for clarity

The free strain was calculated by dividing the change in actuator length by the initial actuator length (Eq. 4). The blocking force, was calculated by multiplying the stress by the MFC's cross sectional area normal to the axis of elongation, in the z direction in Fig. 2 (Eq. 5). Both models were able to predict the free strain and blocking force well, however the thermal model shows superior performance particularly with respect to the free strain with an error of 0.2% and a blocking force error of 7%. It is important to note that if the Navy type II d_{31} coefficient is not incorporated into the model, the accuracy decreases.

$$\varepsilon_{free} = \frac{\Delta L}{L} * 10^{-6} \tag{4}$$

$$F_{block} = \sigma * t * w \tag{5}$$

When choosing the appropriate model, it is necessary to consider not only the accuracy but also the robustness. In the piezoelectric model, the dielectric coefficient of the total MFC is based upon the number of units along the fiber length while the voltage is taken to be the maximum voltage. This works well for rectangular geometries, but introduces complexities and uncertainties for other geometries where the PZT fiber length, and thus the number of units, is no longer constant and the voltage boundary conditions are more difficult to define. Conversely in the thermal model, the thermal loading is distributed evenly throughout the actuator and both the thermal loading and thermal expansion coefficient are dependent upon the actuator length. This effectively removes any dependence upon fiber length, so long as the length is taken to be the same in both the thermal load and coefficient calculations. Accordingly, the following methods implement the thermal model which was shown to provide better results and was also observed to be more robust when customizing the PZT fiber orientation and geometry.

Table 2: Comparison of FEM results

		F_{block} [N]	ε_{free} [ppm]
	Manufacturer	923	1800
MFC	Abaqus	850.4	1714.1
	% Error	7.9%	4.8%
Thermal	Abaqus	856.7	1804
	% Error	7.1%	0.2%

3.4 Customized Fiber Orientation

- To determine the fiber orientation needed to achieve maximized deflection normal to and orthogonal to the freestream, the thermal model [20] discussed in the prior section was implemented with a 0.001 in. AMS 5519 fully hardened steel substrate. The PZT fiber orientation was optimized manually to maximize the tip deflection in the out-of-plane and transverse directions. By maximizing the out-of-plane deflection, the control effectiveness in zero sideslip was guaranteed for pitch and yaw maneuvers. Furthermore, by maximizing the transverse deflection, the control surface remains effective in large sideslip angles unlike in traditional tailless aircraft control surfaces. It is worth noting that both cannot be maximized entirely without tradeoffs, meaning that the maximum value for the tip deflection in the z direction does not correspond to the maximum tip deflection in the y direction. For this analysis, the optimal fiber orientation was chosen to be 55°. If an aircraft is not expected to exceed a certain value of sideslip, the fiber orientation can be more precisely optimized to reflect this. Both the bioinspired UAV body and the final optimized tail geometry were incorporated into the full UAV model shown in Fig. 1 for static aerodynamic simulations.

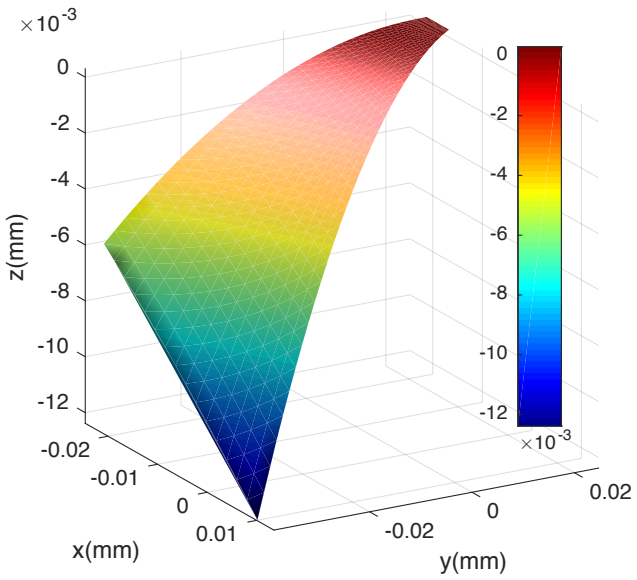

Figure 3. Deformation of custom shaped MFC with 55° rotated fiber orientation

4 Methods

4.1 Actuator Integration

The MFCs were manufactured with the fiber angle determined above and the custom geometry shown in Fig. 1. While this geometry is symmetric, the voltage range and accordingly the actuation range of the MFCs is asymmetric, recall that the minimum voltage is -500 V and the maximum voltage is 1500 V. To demonstrate yaw control and pitch control of this actuator design, symmetric tail actuation is preferable and was achieved by bonding the substrate to the top surface of one MFC, and to the bottom surface of the MFC on the adjacent side. This allowed testing maximum actuations of [1500 V, 0 V] for yaw control, and [1500 V, 1500 V] for pitch control where these configurations represent the right and left actuators. However, this limits the actuation for air brake tests to [-500 V, 500 V].

Each MFC is 0.3mm thick, however in this application some thickness is desired to maintain static yaw stability. For that reason, a substrate was required which provided resistance to out-of-plane loads without restricting the deformation of the MFCs. One method which has been heavily studied are cellular honeycomb structures [22]. A simple method of manufacturing such complex structures is with the aid of 3D printing which is capable of replicating complex geometries with high resolution. The honeycomb used in this work was 3D printed using the multi-material Objet Connex printer which has the ability to combine a rigid digital material with an elastomeric digital material in different ratios to obtain an array of different rigidities. This allows for a multi-part assemblies to be manufactured in a single continuous and integrated print. In this work, it allows the flexible honeycomb substrate to be manufactured with a rigid connection to mount directly to the rest of the aircraft.

4.2 Mechanism Testing

Preliminary testing was conducted on the completed actuator mechanism. The purpose of this testing was to determine the relationship between applied voltage and MFC tip deflection. Measurements were taken using a Keyence LKG-402 laser displacement sensor. The laser displacement sensor was directed at the tip of the MFC and displacement data was collected in increments of 100 volts across the entire operating range of the MFCs. The voltage range of the MFCs is antisymmetric and spans from -500V to 1500V. The results in Fig. 4 show that for this tail geometry, the tail can achieve over ¼ inch of deflection. It is important to note that these results represent the deflection of the actuator upon full integration into the bioinspired UAV, including adhesion to the honeycomb layer. This explains the difference in actuator deflection between the experiments and model. Still, given the size of the model the deflection presented in Fig. 4 is a reasonable magnitude. Furthermore, the relationship between the voltage and out-of-plane tip displacement of the MFC is approximately linear. This linear fit will be used in the latter sections to characterize the yaw moment with respect to the actuator deflection to align with standard convention.

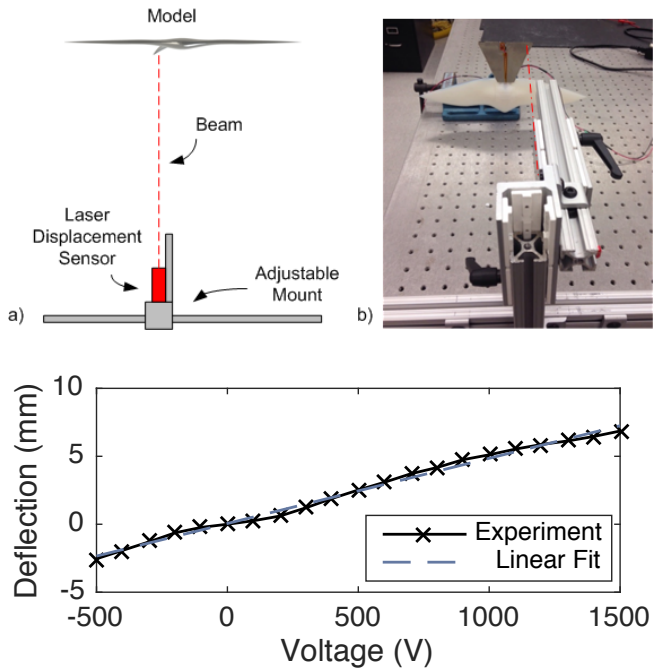

Figure 4. (top) a) Schematic from an aerial view of the experimental setup b) laser displacement sensor setup for measuring relationship between applied MFC voltage and tip displacement **(bottom)** Mechanical characterization of the custom MFC's tip displacement with respect to applied voltage

4.3 Wind Tunnel Setup

Wind tunnel tests were conducted in the 0.6 m x 0.6 m open loop wind tunnel at the University of Michigan. The bioinspired aircraft was 3D printed in Vero White, the most rigid material of the Objet Connex resin products, and was mounted vertically to a ATI Nano17 Titanium 6-axis force balance. While tailless aircraft are typically mounted in wind tunnels using a sting mount, this was determined to be inappropriate for this model because the sting mount would interfere with the horizontal control surface. For this reason, a standard mounting rod through the center of the aircraft body was chosen. Ideally, the mounting rod would be long enough to place the model at the center of the wind tunnel section to guarantee uniform flow; however, due to the size of the model, the force balance could not fit into the aircraft and instead had to be mounted at the top of the wind tunnel. Since the load cell is rated for such small loads to have adequate yaw moment resolution, a long mounting rod would overload the sensor due to torque causing permanent damage. Thus a compromise was reached by placing the model two inches from the wall, well outside of the boundary layer where the flow is approximately uniform.

4.4 Data Acquisition

During the test, temperature, dynamic pressure, and load cell data were recorded and time averaged. Atmospheric temperature within the wind tunnel was recorded by a thermocouple mounted upstream of the model. An Omega PX2650 differential pressure transducer was used to record the dynamic pressure via pitot tubes upstream of the wing. Lastly, the ATI Nano17 Titanium 6-axis load cell was used to record all 3 forces and 3 moments, though in this study

only lift, drag, yaw, and pitch are reported. This sensor has a force resolution of 1/171 N and a torque resolution of 5/184 Nmm in yaw, and 3/182 Nmm in pitch and roll.

The entire experiment was coordinated in MATLAB using a DAQ and dSPACE MicroLabBox for data measurement and actuator control. The DAQ collected data from the thermocouple measuring the temperature inside of the wind tunnel while the dSPACE collected data from all 6 channels of the load cell as well as the differential pressure transducer. No fluid velocity measurements were taken; however, it can be inferred from Bernoulli's principle using the pressure and temperature readings. The data collection algorithm continuously monitored the velocity so that it remained within 5% of the desired velocity.

Furthermore, the dSPACE controlled the output signals throughout the experiment. Two signals were sent to the actuators, one for each side of the actuator. These signals first went to an AVID Dual Channel MFC Bimorph High-Voltage Driver which amplifies a signal between 0 and 5 V to -500 V and 1500V for the MFC actuators. The dSPACE also output the signal to the stepper motor which controlled a rotary table to set the sideslip angle. This allowed the entire experiment to be automated and eliminate human error. A flow diagram of the experiment is depicted in Fig. 4.

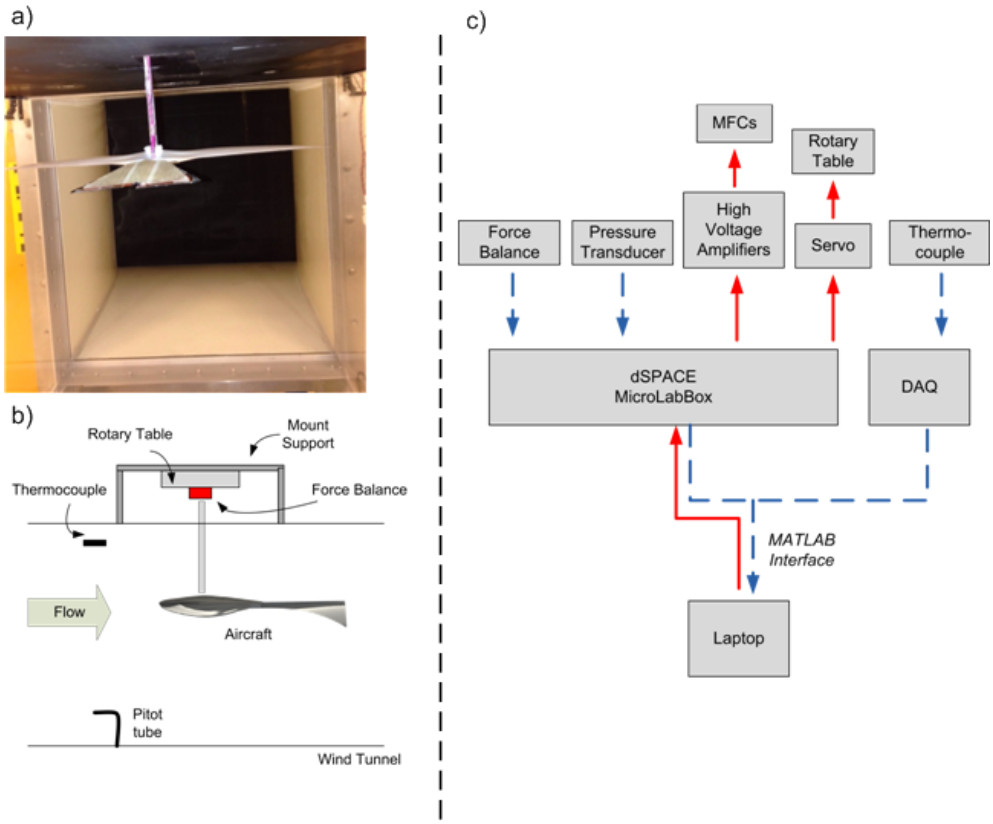

Figure 5. a) Mounted aircraft **b)** schematic of experimental setup **c)** experimental data flow

4.5 Experimental Procedure

Before conducting any tests, the pressure transducer was tared without any air loads and the load cell was tared with the model attached. This established a new zero point given the

weight of the model and the atmospheric conditions which may vary from day to day. Additionally, to account for any errors due to manufacturing tolerance of the mounting setup, a preliminary experiment was conducted with zero tail actuation. Since the aircraft is symmetric, there will be no yaw moment at 0° sideslip angle. Thus, this preliminary test identified the angle offset which was applied to the prescribed sideslip angle in the dSPACE controller. Aerodynamic tests were conducted at 10m/s for a variety of tail configurations: to test the yaw control one MFC was actuated in increments of 250V, to test the pitch control both MFCs were were actuated symmetrically in increments of 250V. To test the air brake capabilities, the MFCs were actuated unsymmetrically at [500, -500].

Upon collecting the aerodynamic forces and moments, the nondimensional aerodynamic coefficients were calculated. The yaw moment coefficient (C_η) was of primary concern for the current work. It is a non-dimensional parameter describing the moment about the vertical axis. In aircraft, this describes the restoring moment experienced by the aircraft in sideslip conditions

$$C_\eta = \frac{N}{\frac{\rho}{2} U^2 S b} \tag{6}$$

where here U is the velocity, ρ is the pressure, N is the yaw moment, b is the half span and S is the reference area. It is important to note the reference quantities used to calculate the nondimensional coefficients used in this analysis. The reference area was chosen to be total wing area which is often used in flying wing or tailless aircraft studies. The characteristic length of the bioinspired wing, used in the calculation of the other aerodynamic coefficients, was calculated as the mean aerodynamic chord shown below

$$MAC = \frac{2}{S} \int_0^{b/2} c^2 dy \tag{Eq.6}$$

where MAC represents the mean aerodynamic chord, and c represents the wing chord at location y. Lastly the yaw moment derivative ($C_{\eta\beta}$) is a metric describing the aircraft's tendency to return to symmetric flight (β=0) when the yaw angle is disturbed. When the derivative is positive, then an increase in sideslip generates a greater yaw moment indicating that the aircraft is stable. For this analysis, this metric is used to ensure that stability is not lost with actuation.

$$C_{\eta\beta} = \frac{\partial C_\eta}{\partial \beta} \tag{7}$$

5 RESULTS AND DISCUSSION

This section presents the results of the aerodynamic testing and a discussion of their implications. The goal was to show that this bio-inspired actuator was capable of providing yaw and pitch control with the potential to act as an air brake.

5.1 Yaw Test

5.1.1 Yaw Moment Coefficient

Figure 6 depicts the yaw moment coefficient for the configurations detailed in Section 3. The unactuated case demonstrates that the yaw moment increases relatively linearly with yaw angle for the angles tested, demonstrating that the horizontal tail alone does provide a restoring yaw moment as observed by Sachs and Hummel. These results were compared to numerical RANS simulations performed using a three dimensional time-steady CFD analysis for low-speed incompressible flow. This required the use of a coupled pressure-based solver which simultaneously solves for the pressure and momentum equations. Due to the low Reynolds number nature of the problem, a suitable turbulence model was critical. Accordingly, a standard k-ω turbulence model was chosen. The experimental data show very good agreement with the simulations, validating the results and ensuring confidence in the latter tests.

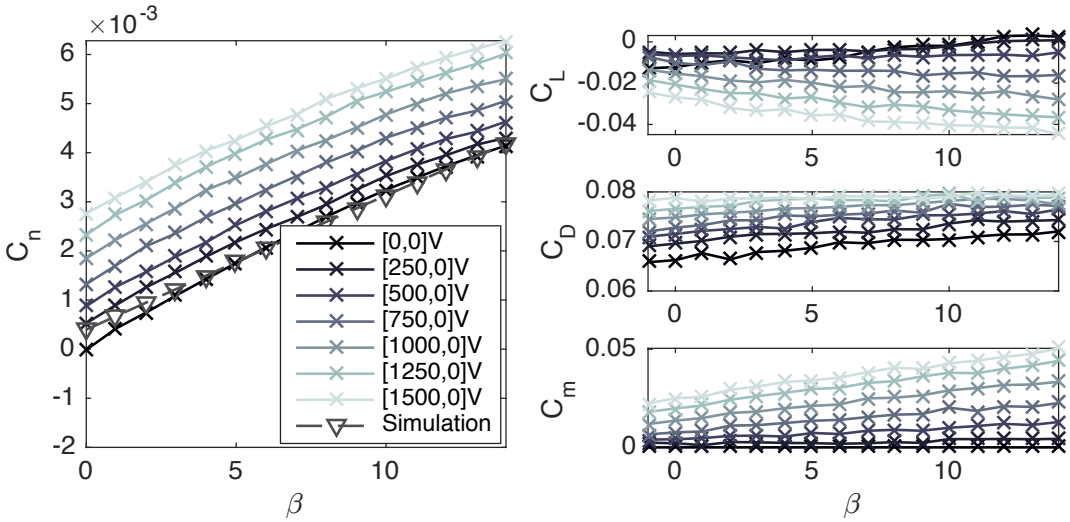

Figure 6. Yaw configuration nondimensional coefficients

Actuating the MFC tail section into the turn increases the yaw moment and remains effective even as sideslip increases. This indicates that not only is the tail effective as a rudder in forward flight, it can also be deployed in sideslip if the static stability characteristics of the tail alone are not enough to restore the aircraft to symmetric flight. The lift, drag, and pitching moment coefficients were also measured to analyze any coupling effects. Overall, the lift remains approximately zero though actuating the control surface with a positive deflection does provide a slight decreasing effect. As expected, the drag increases slightly with increasing deflection since the surface area perpendicular to the flow will increase with sideslip angle. The drag also shows a minor increase with sideslip which can again be attributed to an increase in surface area perpendicular to the flow due to the 3D curvature of the control surface. Lastly, the pitching moment increases with actuation. This is inevitable due to the coupled deformation of the actuator.

5.1.2 Yaw Control Effectiveness

To better understand the effectiveness of the actuator, the yaw coefficient versus actuator tip deflection which was derived from the testing described in section 3 is shown in Fig. 7 for

various sideslip angles. The control effectiveness in symmetric flight shows a quasi-linear increase with actuator deflection. Though comparable in magnitude to the results presented by Stenfelt et al. (2009, 2010), their actuator response was shown to be exponential across multiple sideslip angles which indicates that the actuator has little effectiveness at small to mid range deflections compared to the actuator presented in this study. Therefore, this actuator requires smaller relative deflections to generate the equivalent yaw moment coefficient.

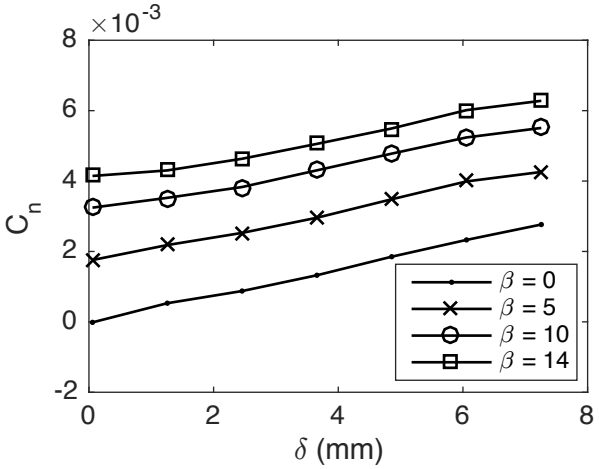

Figure 7. Yaw moment vs. actuator deflection for sideslips ranging from 0° to 14°

Further contrary to those studies, the control effectiveness increases with sideslip angle substantially due to the effect of the tail aspect ratio. Specifically, as the aircraft experiences sideslip, the moment arm of the actuator increases since it lies aft of the center of gravity. One can imagine how having a higher aspect ratio tail would further increase the control effectiveness. Furthermore, the control effectiveness of the tail does not degrade with increasing sideslip which is evident by the constant slope across all sideslip cases. Though not experienced here, a smaller slope would indicate a decrease in effectiveness with sideslip while data that collocated with the symmetric flight results would indicate a lack of contribution of the actuator's aspect ratio.

5.1.3 Yaw Stability

Yaw stability analysis is frequently conducted by prescribing a specified sideslip and sweeping through a series of pitch angles to vary the lift. The experimental setup detailed in section 3 was only capable of commanding one degree of freedom as opposed to both yaw and pitch; however, the yaw stability at 0° pitch angle can be inferred from the data presented in Fig. 6. As noted prior, the slope of the yaw moment coefficient remains practically constant across all sideslips and tip deflection, indicating that the yaw moment derivative for the unactuated and actuated configurations are equal within the range of sideslip angles tested. By taking the derivative, the magnitude of the yaw moment stability was calculated to be near 0.01, larger than other reported stability derivatives. As this value is positive, it demonstrates stability in both the unactuated and actuated configurations at 0° pitch angle.

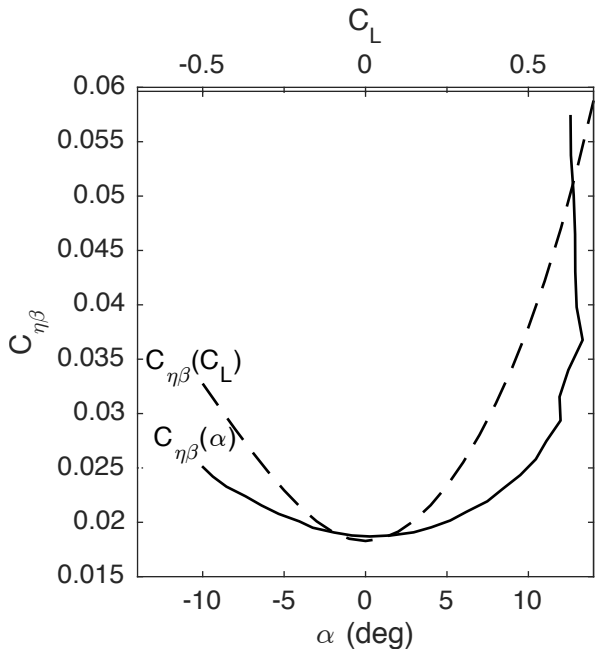

Figure 8. Yaw moment vs. angle of attack and lift coefficient for $\beta = 10°$

Additionally, using the RANS model for the unactuated geometry presented prior, the stability derivate can be modeled numerically for further analysis. A 10° sideslip was prescribed while the angle of attack was varied. The data presented in Fig. 8 show that the tail geometry alone acts as a static yaw stabilizer since the positive increase in yaw moment acts to restore the attitude of the aircraft towards symmetric flight, confirming the findings of other works cited here [4]. Even in dive maneuvers, when the angle of attack is negative, the stability derivative remains positive. Since it was shown that actuating the tail increases the yaw moment coefficient, it is reasonable to conclude that stability is not lost in the actuated configurations.

5.1.4 Pitch Control

The pitching moment is more complex. Typically, the pitching moment of a straight wing is measured about the quarter chord as the wing changes angle of attack. In this work, not only are the wings tapered nonuniformly, but the mounting rod between the aircraft and load cell acts as a moment arm which increases the measured pitching moment readings. The tapered wing has been addressed in the prior discussion of reference values used in calculating the nondimensional parameters. However, to address the biased readings due to the mounting rod, some data processing must be incorporated. Since the goal in this analysis is to quantify how much the tail affects the pitching moment, a simple solution is to subtract the measured pitching moment coefficient for the unactuated configuration from the other datasets. This will directly show the contribution to pitching moment due to the actuated control surface. This post-processing was also applied to the pitching moment data discussed above.

Figure 8 presents the nondimensional aerodynamic coefficients for the symmetrically actuated tail to control pitch. The data show that the pitching moment increases with tail actuation regardless of the sideslip angle. Furthermore, the effects of the tail on pitching moment remain relatively constant over the range of sideslips tested. It should be noted that the pitching

moment coefficient for these configurations is approximately twice the pitching moment experienced with only one MFC actuated, as in the yaw control experiment conducted prior. Again, the lift remains zero with a slight decrease with actuation. The drag remains relatively constant as well, though it experiences a unique trend. When the tail is symmetrically actuated, the drag decreases with sideslip. Since the normal vector of the left MFC turns away from the free stream flow with increasing sideslip, the area of that control surface decreases. Due to the shape of the control surface and the orientation of the PZT fibers in the MFC, the decrease in the effective area of the left control surface exceeds the increase in effective area of the right control surface causing an overall reduction in drag with sideslip for the range of angles tested. Lastly, since the MFCs were actuated symmetrically, the yaw moment at zero degrees for all cases should be equal to zero. For these configurations, the yaw moment becomes slightly negative with increasing actuation. This indicates that perhaps the MFCs are not actuating entirely symmetrically and supports the incorporation of a displacement sensor to guarantee exact displacements for future experiments.

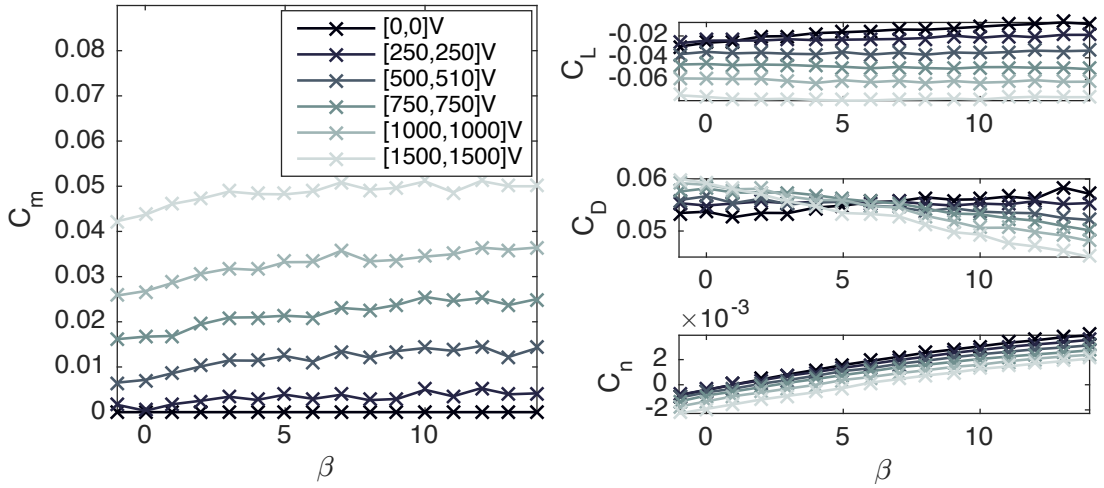

Figure 7. Pitch control nondimensional coefficients

5.1.5 Air Brake Control

Finally, the results of the air break analysis are presented in Fig. 9. Given the limited effect of actuation on drag in the previous experiments, only the case with maximum deflection was tested to determine whether using this morphing mechanism as an air break is feasible. Although the drag does increase for the [500,-500] case shown below, it does not appear significant compared to the typical increase in drag coefficient with air brakes or drag rudders which well exceeds 0.05. Even if the tail had full voltage range [1500,-1500], the increase in drag coefficient would only be approximately 0.045 assuming that it scales linearly. This indicates that the current configuration would not be adequate as an air break. However, if the control surface area could be increased further when actuated, this might still be possible. This could be achieved if more of the deformation was in the out of plane direction. One possible solution might be to use a bimorph configuration with a 55° MFC layer and a 0° MFC layer which would allow the control surface shape to be further customizable in flight. To deploy the air break, the 0° layer would be actuated which would generate a 2D cambered shape like the cascading bimorph concept, maximizing the control surface area perpendicular to the free stream flow, though it

would have a more dramatic effect on pitching moment. This replicates how birds pitch their tails down during landing maneuvers to rapidly decrease speed. Furthermore, both the 55° and 0° layers could be actuated independently to tailor the in plane and out of plane deformations of the tail during yaw and pitch maneuvers.

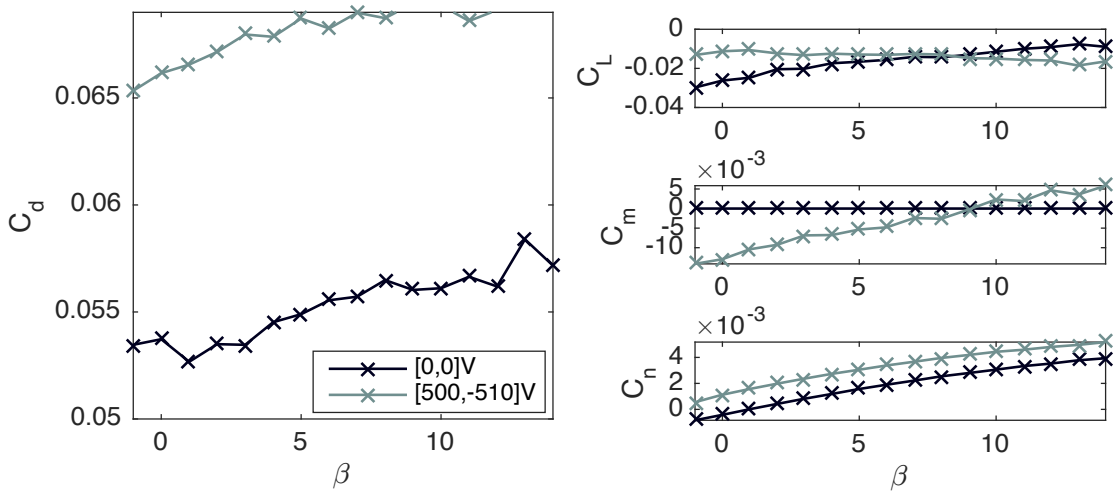

Figure 8. Air brake control nondimensional coefficients

6 Conclusion

In this work, a novel bioinspired actuator for a tailless UAV was developed. The 3D deformations of the actuator, a by-product of bending-twisting coupling, was achieved using custom designed MFCs with rotated fiber orientation with the intention of maintaining if not increasing control effectiveness of yaw in sideslip conditions. A flexible honeycomb structure was also incorporated to seamlessly integrate the control surface into the bioinspired aircraft. The deflection of the actuator was characterized before conducting wind tunnel tests to determine its aerodynamic capabilities. Single sided actuation was conducted to test yaw performance, symmetric actuation was conducted to test pitch performance, and antisymmetric actuation was conducted to test air break performance. The control surface was shown to effectively increase the yaw and pitching moment for positive actuation, indicating that

a) in the event that the static stability characteristics of the tail alone are insufficient in restoring forward flight during sideslip, one side of the tail can deploy to significantly increase the restoring yaw moment

b) even in forward flight, the tail is capable of generating a yaw moment which can be used as small amplitude corrective input for dynamic stabilization

c) the aircraft is able to control pitch as both dynamic stabilization during forward flight, and largescale attitude control even in sideslip

While experiments to characterize the air brake qualities of this control surface were conducted, the effect was shown to be insignificant. However, it offers insight into methods of improving this design in future iterations. This could include using a bimorph configuration where the 2nd MFC layer would have a 0° fiber orientation. These MFCs could be actuated independently, allowing for more tailored control over the curvature of the control surface. By

actuating the 0° MFCs alone, the curvature would be strictly 2D and would increase the pitching moment coefficient and could also be used in braking maneuvers as birds do while landing. Alternately, for yaw control one of the 55° MFCs could be actuated alone or in unison with the 0° MFC to tune the 3D curvature to suit the sideslip conditions.

ACKNOWLEDGMENTS

This work is supported in part by the US Air Force Office of Scientific Research under a grant number FA9550-16-1-0087, titled ‘Avian-Inspired Multifunctional Morphing Vehicles’’ monitored by Dr. BL Lee.

7 Works Cited

[1] A. C. Carruthers, A. L. Thomas and G. K. Taylor, "Automatic aeroelastic devices in the wings of a steppe eagle Aquila nipalensis," *Journal of Experimental Biology,* vol. 210, no. 23, pp. 4136-4149, 2007.

[2] J. A. Gillies, A. L. Thomas and G. K. Taylor, "Soaring and manoeuvring flight of a steppe eagle Aquila nipalensis," *Journal of Avian Biology,* vol. 42, no. 5, pp. 377-386, 2011.

[3] D. Lentink, U. K. Muller, E. J. Stamhuis, R. De Kat, W. Van Gestel, L. M. Veldhuis, P. Henningsson, A. Hedenstrom, J. J. Videler and J. L. Van Leeuwen, "How swifts control their glide performance with morphing wings," *Nature,* vol. 7139, no. 446, pp. 1082-1085, 2007.

[4] G. Sachs, "Tail effects on yaw stability in birds," *Journal of Theoretical Biology,* vol. 293, no. 3, pp. 464-472, 2007.

[5] D. Hummel, "Aerodynamic investigations on tail effects in birds," *Zeitschrift für Flugwissenschaften und Weltraumforschung,* vol. 16, pp. 159-168, 1992.

[6] G. Cai, K. Y. Lum, B. M. Chen and H. Lee T, "A brief overview on miniature fixed-wing unmanned aerial vehicles," in *8th IEEE International Conference on Control and Automation (ICCA)*, 2010.

[7] G. Stenfelt and U. Ringertz, "Yaw control of a tailless aircraft configuration," *Journal of Aircraft,* vol. 47, no. 5, p. 1807, 2010.

[8] B. Jeong, D. Lee, H. Shim, J. Ahn, H. L. Choi, S. O. Park and S. Y. Oh, "Yaw-Control Spoiler Design Using Design of Experiments Based Wind Tunnel Testing," *Journal of Aircraft,* vol. 52, no. 2, pp. 713-718, 2014.

[9] G. Stenfelt and U. Ringertz, "Lateral stability and control of a tailless aircraft configuration," *Journal of Aircraft,* vol. 46, no. 6, pp. 2161-2163, 2009.

[10] S. Barbarino, O. Bilgen, R. M. Ajaj, M. I. Friswell and D. J. Inman, "A Review of Morphing Aircraft," *Journal of intelligent material systems and structures,* vol. 22, no. 9, pp. 823-877, 2011.

[11] O. Bilgen, K. B. Kochersberger, D. J. Inman and O. J. Ohanian III, "Novel, Bidirectional, Variable-Camber Airfoil via Macro-Fiber Composite Actuators," *Journal of Aircraft,* vol. 47, no. 1, p. 303, 2010.

[12] A. M. Pankonien and D. J. Daniel, "Aerodynamic Performance of a Spanwise Morphing Trailing Edge Concept," in *25th International Conference on Adaptive Structures and Technologies*, The Hauge, 2014.

[13] A. M. Pankonien and D. J. Daniel, "Experimental Testing of Span-wise Morphing Trailing Edge Concept," in *Proceedings of SPIE active and passive smart structures and integrated systems*, San Diego, 2013.

[14] L. L. Gamble, A. M. Pankonien and D. J. Daniel, "Stall Recovery of the Span-wise Morphing Trailing Edge Concept via an Optimized Nonlinear Model," in *26th International Conference on Adaptive Structures and Technologies*, Kobe.

[15] S. Kota, J. Hetrick, R. Osborn, D. Paul, E. Pendelton, P. Flick and C. Tilmann, "Design and application of compliant mechanisms for morphing aircraft structures," in *Proceedings of SPIE* , 2003.

[16] R. Guiler and W. Huebsch, "Wind tunnel analysis of a morphing swept wing tailless aircraft," in *23rd AIAA Applied Aerodynamics Conference*, Toronto, 2005.

[17] D. R. Bye and P. D. McClure, "Design of a morphing vehicle," in *48th AIAA Structures, Structural Dynamics, and Materials Conference*, Honolulu, 2007.

[18] J. D. Anderson, Fundamentals of aerodynamics, New York: McGraw-Hill Education, 2010.

[19] J. Latalski, "Modelling of macro fiber composite piezoelectric active elements in ABAQUS system," *Maintainence and Reliability,* vol. 4, pp. 72-78, 2011.

[20] F. Cote, P. Masson, N. Mrad and V. Cotoni, "Dynamic and static modelling of piezoelectric composite structures using a thermal analogy with MSC/NASTRAN," *Composite Structures,* vol. 65, no. 3, pp. 471-484, 2004.

[21] I. o. E. a. E. E. Inc., "IEEE standard on piezoelectricity," ANSI/IEEE , 1988.

[22] K. R. Olympio and F. Gandhi, "Flexible skins for morphing aircraft using cellular honeycomb cores," *Journal of intelligent material systems and structures,* vol. 21, no. 17, pp. 1719-1735, 2010.